Advanced Modeling of SIW Structures by 2D Finite Element Method

L. Codecasa, *Member, IEEE*, C. D'Asta, G. G. Gentili, M. Bozzi, *Fellow, IEEE*, L. Perregrini, *Fellow, IEEE*

***Abstract*—This paper presents an advanced modeling of Substrate Integrated Waveguide (SIW) structures by 2D vector Finite Element Method (FEM). All types of losses are considered, together with input/output coupling by rectangular waveguide and coaxial cable. Multiple dielectric regions can be defined, allowing the modeling of partially air-filled SIW structures with excellent accuracy and efficiency.**

Keywords: ***Finite element method (FEM), microwave filters, substrate integrated waveguide (SIW).***

I. Introduction

SUBSTRATE Integrate Waveguide (SIW) has consolidated as an extremely attractive technology because of its low cost, simple fabrication ad good compromise between performance and easy integration with on-chip components [1]–[6]. SIW structures offer flexible design features, such as strong miniaturization (achieved by the use of a high permittivity) and the possibility to easily alternate vacuum regions and dielectric filled regions [3], increasing the quality factor and providing additional design flexibility in SIW filters with complex transfer functions implementing transmission zeros [2] or in new applications for slow wave components [4].

In spite of the planarity of SIW structures, in the literature the full-wave modeling often resorts to full 3D Finite Element Method (FEM), especially because of its capability to model losses and coaxial-type input. Owing to the reduced thickness of SIW structures, losses often play a significant role and as a general rule they cannot be neglected. However, the independency of the fields with respect to the out-of-plane coordinate allows in principle SIW components to be analyzed by 2D codes. In [7], [8] and [9] 2D-FEM was used, but losses were not considered because of the use of the scalar formulation which uses as a variable the out-of-plane component of the electric field. Moreover, only waveguide input was considered. In [10] and [11] equivalent square posts were used to simulated the circular posts, and this allowed the use of an efficient 2D mode-matching technique (MM). This permits a fast analysis of some devices, but with MM complex shapes are hard to implement and partially air-filled regions are even more challenging. In those papers, losses were introduced either by an equivalent lossy material [10] or by asymptotic boundary conditions [11]. Methods based on Green's function with some modifications to include losses have been successfully used in [13], [14], [15], with very good efficiency, but partially filled air regions of general shape were not presented. With those techniques, partially air filled regions are complex to implement because they require a segmentation of the structure and a consequent increase of the computation time. In [16] air-filled region of circular shape have been modeled by a cylindrical mode expansion. That technique, although very efficient too, was not applied to arbitrarily shaped air regions and losses were not modeled.

L. Codecasa, C. D'Asta, G. G. Gentili are with Dipartimento di Elettronica, Informazione e Bioingegneria, p.za L. da Vinci 32, Milano (Italy). mailto: gianguido.gentili@polimi.it. M. Bozzi, L. Perregrini are with University of Pavia, Pavia (Italy)

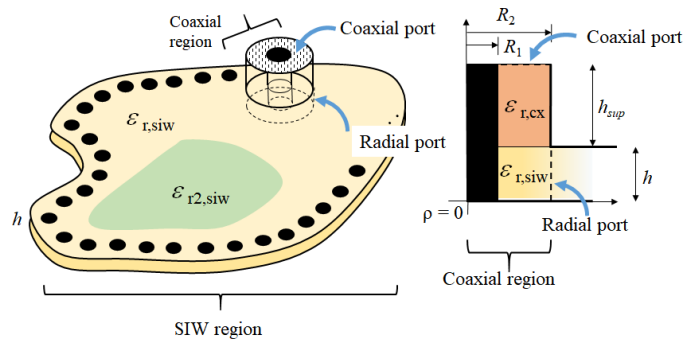

Fig. 1. A sketch of the SIW structure with coax-type input. The structure is divided into two regions, SIW region and coaxial region, separated by a radial port.

In [5] SIW were analyzed by 2D version of BI-RME and losses were included by introducing a quality factor for each mode in the modal expansion of BI-RME. Although this technique is very efficient, again the analysis of partially air-filled SIW structure by BI-RME is difficult, because it requires a segmentation of the device and a further connection of the partial admittance matrices, similarly to what reported in [17] in which a general segmentation technique is discussed combining 3D FEM and addition theorem with cylindrical wave functions.

In order to overcome some limitations in the available literature and to increase the efficiency of the analysis, in this work we propose a vector 2D FEM modeling of SIW that uses the magnetic field component as the unknown [20]. Although vector FEM is slightly less efficient than scalar FEM for equal degree of the shape functions, we show that with the vector formulation we can easily model all losses present in the structure. Partially air-filled regions can be very easily introduced in the structure with no increase of the problem size and, thanks to the simple circular arc shape element obtained by coordinate transformation [24], perfectly circular posts are easily implemented in our code without the need of isoparametric elements. Finally, input and output of waveguide type and coaxial type are also modeled in the

frame of the 2D formulation, thanks to the use of a very efficient decomposition of the structure obtained using a radial admittance matrix approach for the coaxial region (see e.g. [22]). As a whole, thanks to the 2D analysis, a remarkable accuracy and efficiency has been obtained. Validation of the results by comparison with full 3D code for several SIW components has been carried out and discussed in this paper.

The organization of the paper is the following: we present the formulation in section II, outlining all necessary boundary and volume terms accounting for all types of losses. The discretization of the SIW structure is presented in section III, together with the computation of the admittance matrices. In section IV we discuss in more detail the port terms and in particular the important problem of excitation by coaxial ports. For these, we present a 2.5D radial FEM formulation in cylindrical coordinates. The final admittance matrix for the final structure is obtained by block connection of partial admittance matrices at common radial ports (section V). Some examples are finally discussed in section VI, comprising filters with homogeneous materials, air-filled cavities and a comparison with measured results. A final section presents some conclusions and summarizes the results obtained.

II. Formulation

A quick review of magnetic field formulation of FEM is now presented for clarity, with a description of the various terms that contribute to the final linear system of equations. We start assuming that the SIW structure is placed in xy plane and has a thickness h (Fig. 1). Fields are independent of z by hypothesis, so that

$$\boldsymbol{E}(x,y,z) = \boldsymbol{i}_z E_z(x,y) \tag{1}$$

$$\boldsymbol{H}(x,y,z) = \boldsymbol{H}_t(x,y) = \boldsymbol{i}_x H_x(x,y) + \boldsymbol{i}_y H_y(x,y) \tag{2}$$

where $\boldsymbol{i}_x, \boldsymbol{i}_y, \boldsymbol{i}_z$ are the unit vectors along the coordinate axes and the subscript t indicates transverse-to-z component. Letting then ∇_t be the transverse Nabla operator and being by hypothesis $\partial/\partial z = 0$ for all fields, we state the problem as follows: we look for $\boldsymbol{H}_t$ such that

$$\int_V \nabla_t \times \boldsymbol{T} \cdot \bar{\boldsymbol{\epsilon}}_r^{-1} \nabla_t \times \boldsymbol{H}_t dV - k_0^2 \int_V \boldsymbol{T} \cdot \bar{\boldsymbol{\mu}}_r \boldsymbol{H}_t dV + \\ - \int_{\partial V} \boldsymbol{T} \cdot (\bar{\boldsymbol{\epsilon}}_r^{-1} \nabla_t \times \boldsymbol{H}_t) \times \boldsymbol{i}_\nu dS = 0, \\ \forall \boldsymbol{T} \in H(\mathrm{curl}, V) \tag{3}$$

where $H(\mathrm{curl}, V)$ is the Sobolev space of vector functions that are square integrable in V together with their curl. In (3) $\boldsymbol{i}_\nu$ is the unit vector normal to the volume and outward drawn, $\bar{\boldsymbol{\epsilon}}_r$ is the relative permittivity tensor, $\bar{\boldsymbol{\mu}}_r$ is the relative permeability tensor, k_0 is the free space wavenumber and ∂V is the boundary of volume V.

Since we are mostly interested in the case of permittivity and permeability being scalar functions of position, we can write

$$\bar{\boldsymbol{\epsilon}}_r = \epsilon_r \bar{\boldsymbol{\Lambda}}, \qquad \bar{\boldsymbol{\mu}}_r = \mu_r \bar{\boldsymbol{\Lambda}} \tag{4}$$

in which $\bar{\boldsymbol{\Lambda}}$ is the equivalent anisotropic material originating from the coordinate transformation that yields perfectly circular arc elements in a triangular 2D mesh (see [24] for details).

We then split the boundary ∂V into four terms: the ports (∂V_{p}), the conductors surface of the vias ($\partial V_{\mathrm{via}}$), the upper and lower metal planes ($\partial V_{u,l}$) and the outer boundary ($\partial V_{\mathrm{ext}}$). Unlike losses in the dielectric, that can be accounted for by introducing a complex permittivity $\epsilon_r = \epsilon_r'(1 - j\tan\delta_\epsilon)$, being $\tan\delta_\epsilon$ the loss tangent of the dielectric material, losses due to finite conductivity conductors or radiation require specific boundary terms. We start defining all these boundary terms and then define the discretization and the solution process for the computation of the admittance matrix.

Port term is defined in detail in section IV, since the case of coaxial type input requires a further FEM discretization.

A. Boundary Terms for the Vias and for the Upper and Lower Conductors

For the metallic part of the boundary we can use the well known Leontovich boundary condition [18] and write on $\partial V_{\mathrm{via}}$ and on $\partial V_{u,l}$

$$\boldsymbol{i}_\nu \times \boldsymbol{E} = Z_s \boldsymbol{i}_\nu \times (\boldsymbol{H} \times \boldsymbol{i}_\nu) \tag{5}$$

where $Z_s = (1+j)\sqrt{\omega\mu/(2\sigma)}$, being σ the metal conductivity. We use the customary perturbative hypothesis that assumes that the magnetic field variation due to finite conductivity is a small fraction of the field in the lossless case. Letting $\boldsymbol{E}', \boldsymbol{H}'$ the fields in the lossless case and $\boldsymbol{E} = \boldsymbol{E}' + \delta\boldsymbol{E}, \boldsymbol{H} = \boldsymbol{H}' + \delta\boldsymbol{H}$ the fields for the lossy case, we have that on the metallic boundaries

$$\boldsymbol{i}_\nu \times \boldsymbol{E} = \boldsymbol{i}_\nu \times (\boldsymbol{E}' + \delta\boldsymbol{E}) = \boldsymbol{i}_\nu \times \delta\boldsymbol{E} \tag{6}$$

since $\boldsymbol{i}_\nu \times \boldsymbol{E}' = 0$ and being

$$j\omega\epsilon_0 \delta\boldsymbol{E} \times \boldsymbol{i}_\nu = (\bar{\boldsymbol{\epsilon}}_r^{-1} \nabla \times \boldsymbol{H}) \times \boldsymbol{i}_\nu \tag{7}$$

we can write

$$-(\bar{\boldsymbol{\epsilon}}_r^{-1} \nabla \times \boldsymbol{H}) \times \boldsymbol{i}_\nu = j\omega\epsilon_0 Z_s \boldsymbol{i}_\nu \times (\boldsymbol{H} \times \boldsymbol{i}_\nu). \tag{8}$$

By noting that the fields are z-independent and that $\boldsymbol{i}_\nu = \pm\boldsymbol{i}_z$, we have $\bar{\boldsymbol{\epsilon}}_r^{-1}(\nabla \times \boldsymbol{H}) \times \boldsymbol{i}_\nu = \bar{\boldsymbol{\epsilon}}_r^{-1}(\nabla_t \times \boldsymbol{H}_t) \times \boldsymbol{i}_\nu$ and $\boldsymbol{H} \times \boldsymbol{i}_\nu = \boldsymbol{H}_t \times \boldsymbol{i}_\nu$. The corresponding boundary term in the weak form becomes therefore, for the vias

$$-\int_{\partial V_{\mathrm{via}}} \boldsymbol{T} \cdot (\bar{\boldsymbol{\epsilon}}_r^{-1} \cdot \nabla_t \times \boldsymbol{H}_t) \times \boldsymbol{i}_\nu dS = \\ j\omega\epsilon_0 Z_{s,\mathrm{via}} h \int_{L_{\mathrm{via}}} \boldsymbol{T} \cdot [\boldsymbol{i}_\nu \times (\boldsymbol{H}_t \times \boldsymbol{i}_\nu)] dl \tag{9}$$

where L_{via} is the 2D boundary of the vias, and for the upper and lower plates

$$-\int_{\partial V_{u,l}} \boldsymbol{T} \cdot (\bar{\boldsymbol{\epsilon}}_r^{-1} \cdot \nabla_t \times \boldsymbol{H}_t) \times \boldsymbol{i}_\nu dS = 2j\omega\epsilon_0 Z_s \int_S \boldsymbol{T} \cdot \boldsymbol{H}_t dS \tag{10}$$

where S is the 2D surface of the SIW structure in xy plane. The factor '2' accounts for the equal contribution of the upper and lower surface. Note that the surface impedance for the vias was set to $Z_{s,\mathrm{via}}$ that can be different from Z_s for the upper and lower conductor because vias could be realized with a different material. Eq. (10) was never previously used to the authors' knowledge to compute losses in SIW.

B. Outer Boundary Term

Thanks to the flexibility of FEM, different outer boundary conditions can be easily implemented. The case of perfect magnetic conductor (PMC) is obtained by eliminating the unknowns corresponding to edges on the external boundary. For most purposes, this is the most convenient boundary condition because it reduces the size of the problem. A well designed arrangement of vias together with PMC side walls is the most convenient modelization of SIW.

In order to take into account possible leakage through the boundary, an impedance boundary condition of the type

$$\boldsymbol{i}_\nu \times \boldsymbol{E} = \eta_{\text{ext}} \boldsymbol{i}_\nu \times (\boldsymbol{H} \times \boldsymbol{i}_\nu) \tag{11}$$

can be implemented very easily too. In (11) η_{ext} represents in equivalent form leakage by radiation and local reactive energy storage. Since a good design should try to minimize leakage as much as possible [5], the contribution of this term to losses is generally extremely small. An approximate expression for η_{ext} can be obtained by the slot admittance formulas originally derived for microstrip patch antennas, in which a resistive term accounts for radiation and a capacitive term represents excess capacitance due to fringing fields [19]. Its expression, slightly simplified and modified so as to represent a local field ratio, reads in our case

$$\frac{1}{\eta_{\text{ext}}} = \frac{h}{120\lambda_0} + j\omega\epsilon_0\epsilon_r h\, 0.412 \frac{\epsilon_r + 0.3}{\epsilon_r - 0.258} \tag{12}$$

where λ_0 is the free space wavelength and ϵ_r is the dielectric constant of the SIW. Expression (12) is clearly approximate and its purpose is to model the effects of widely spaced vias, a condition that should not be used in practice. The use of (12) allows anyway to outline possible spurious radiation effects in the SIW and it introduces a very small additional computational effort.

An alternative is represented by the use of artificial ports connected to fictitious waveguides, as previously discusses in [12]. This type of boundary condition is capable to model attenuation due to radiation in a SIW waveguide, but leads to a large number of modes with consequent larger computation time. For a description of this case, we refer to the following subsection, in which we define the port terms corresponding to waveguide inputs. For the case of impedance loading, which is our preferred approach, the corresponding boundary term is

$$\begin{aligned} -\int_{\partial V_{\text{ext}}} \boldsymbol{T} \cdot (\bar{\boldsymbol{\epsilon}}_r^{-1} \cdot \nabla_t \times \boldsymbol{H}_t) \times \boldsymbol{i}_\nu dS = \\ j\omega\epsilon_0\eta_{\text{ext}} h \int_{L_{\text{ext}}} \boldsymbol{T} \cdot [\boldsymbol{i}_\nu \times (\boldsymbol{H}_t \times \boldsymbol{i}_\nu)] dl. \end{aligned} \tag{13}$$

where L_{ext} is the outer boundary of the SIW structure.

C. The 2D Equation in the SIW Region

We are now able to setup the complete 2D weak form for magnetic field accounting for all types of losses. The boundary terms relative to the ports are discussed in more detail in the following sections. To proceed, we divide all terms by h and move the port term to the right of the equal sign. Moreover, at the ports we let

$$(\bar{\boldsymbol{\epsilon}}_r^{-1} \nabla_t \times \boldsymbol{H}_t) \times \boldsymbol{i}_\nu = j\omega\epsilon_0 \boldsymbol{E}_\xi \times \boldsymbol{i}_\nu \tag{14}$$

where $\boldsymbol{E}_\xi$ is an applied electric field. We therefore look for $\boldsymbol{H}_t$ such that

$$\begin{aligned} \int_S \nabla_t \times \boldsymbol{T} \cdot \bar{\boldsymbol{\epsilon}}_r^{-1} \nabla_t \times \boldsymbol{H}_t dS - k_0^2 \int_S \boldsymbol{T} \cdot \bar{\boldsymbol{\mu}}_r \boldsymbol{H}_t dS + \\ j\omega\epsilon_0 Z_{s,\text{via}} \int_{L_{\text{via}}} \boldsymbol{T} \cdot [\boldsymbol{i}_\nu \times (\boldsymbol{H}_t \times \boldsymbol{i}_\nu)] dl + \\ j\omega\epsilon_0\eta_{\text{ext}} \int_{L_{\text{ext}}} \boldsymbol{T} \cdot [\boldsymbol{i}_\nu \times (\boldsymbol{H}_t \times \boldsymbol{i}_\nu)] dl + \\ \frac{2j\omega\epsilon_0 Z_s}{h} \int_S \boldsymbol{T} \cdot \boldsymbol{H}_t dS = j\omega\epsilon_0 \int_{L_p} \boldsymbol{T} \cdot (\boldsymbol{E}_\xi \times \boldsymbol{i}_\nu) dl \\ \forall \boldsymbol{T} \in H(\text{curl}, S) \end{aligned} \tag{15}$$

where S is the surface of the SIW structure in xy plane and L_p is the segment or collection of segments representing the port. Eq. (15) is the final 2D weak form for magnetic field, in which only surface integrals or line integrals appear.

III. FEM Discretization in the SIW and Admittance Matrix Computation

When the structure is fed by waveguide ports only, we only deal with the discretization and subsequent admittance computation of (15). In case of coaxial type input, solving (15) is an intermediate step for the computation of the final admittance matrix.

For the discretization of (15) we use first order or second order edge elements [20]. So we write the magnetic field in the SIW region as

$$\boldsymbol{H}_t = \sum_q I_q \boldsymbol{\tau}_q(x, y) \tag{16}$$

where $\boldsymbol{\tau}_q(x, y)$ is the generic edge element and the I_q are unknown coefficients. Using the same $\boldsymbol{\tau}_q$ as testing functions (Galerkin's method), we obtain the following matrix equation

$$\begin{aligned} \Big\{ \mathbf{A} - k_0^2 \mathbf{B} + j\omega\epsilon_0 \Big[Z_s \mathbf{C}_{\text{via}} + \frac{2Z_s}{h} \mathbf{C}_u + \eta_{\text{ext}} \mathbf{C}_{\text{ext}} \Big] \Big\} \mathbf{I} \\ = j\omega\epsilon_0 \mathbf{C}_p \end{aligned} \tag{17}$$

in which $\mathbf{I} = [I_1\ I_2 \ldots]^{\text{T}}$ is the vector of unknown coefficients and the matrix elements are defined by

$$\mathbf{A}(p, q) = \int_S \frac{1}{\epsilon_r} \nabla_t \times \boldsymbol{\tau}_p \cdot \bar{\boldsymbol{\Lambda}}^{-1} \nabla_t \times \boldsymbol{\tau}_q dS \tag{18}$$

$$\mathbf{B}(p, q) = \int_S \mu_r \boldsymbol{\tau}_p \cdot \bar{\boldsymbol{\Lambda}} \boldsymbol{\tau}_q dS \tag{19}$$

$$\mathbf{C}_{\text{via}}(p, q) = \int_{L_{\text{via}}} \boldsymbol{\tau}_p \cdot [\boldsymbol{i}_\nu \times (\boldsymbol{\tau}_q \times \boldsymbol{i}_\nu)] dl \tag{20}$$

$$\mathbf{C}_u(p, q) = \int_S \boldsymbol{\tau}_p \cdot \boldsymbol{\tau}_q dS \tag{21}$$

$$\mathbf{C}_{\text{ext}}(p, q) = \int_{L_{\text{ext}}} \boldsymbol{\tau}_p \cdot [\boldsymbol{i}_\nu \times (\boldsymbol{\tau}_q \times \boldsymbol{i}_\nu)] dl \tag{22}$$

$$\mathbf{C}_p(p, \xi) = \int_{L_p} \boldsymbol{\tau}_p \cdot (\boldsymbol{E}_\xi \times \boldsymbol{i}_\nu) dl. \tag{23}$$

The solution of (17) allows to compute the admittance matrix $\mathbf{Y}$ of the structure. Rewriting (17) as

$$\mathbf{L}\mathbf{I} = j\omega\epsilon_0 \mathbf{C}_p \tag{24}$$

one finds

$$\mathbf{I} = j\omega\epsilon_0 \mathbf{L}^{-1}\mathbf{C}_p \tag{25}$$

which is the "short-circuit" magnetic field, from which, by testing with the port mode functions, one finds the admittance matrix $\mathbf{Y}$. The final expression is

$$\mathbf{Y} = \mathbf{C}_p^{\mathrm{T}}\mathbf{I} = j\omega\epsilon_0 \mathbf{C}_p^{\mathrm{T}}\mathbf{L}^{-1}\mathbf{C}_p. \tag{26}$$

Matrix $\mathbf{Y}$ is the final admittance matrix when only waveguide ports are present in the structure and we only have to specialize the forcing term $\boldsymbol{E}_\xi$. The case of coaxial type input is more complex and matrix $\mathbf{Y}$ is just an intermediate result. These two cases are now discussed.

IV. Port Terms

We can have two type of port terms: rectangular waveguide port and coaxial port. We now specialize the forcing electric field $\boldsymbol{E}_\xi$ to these two cases.

A. Rectangular waveguide port

For a rectangular waveguide port we can write

$$\boldsymbol{E}_\xi = \boldsymbol{i}_z E_n = \boldsymbol{i}_z \sqrt{\frac{2}{a}} \sin\frac{n\pi s}{a} \tag{27}$$

being s a coordinate local to the port and a the port size. Eq. (27) defines the field of TE_{n0} mode in the input/output waveguide, n being the mode index. In order to properly describe the field at the waveguide ports, several modes can be used as input/output. Waveguide ports can also efficiently model "SIW" ports, in which an effective waveguide size in used to simulated a SIW waveguide connected to input/output port, as discusses in [1] and [21].

B. Coaxial Port

In the literature, coaxial excitation is often modeled by a simple pin with an impressed current. We found that this model is only valid at very low frequencies, and thus we developed a better model that holds its validity up to much higher frequencies. We divide the SIW structure in two regions as shown in Fig. 1, a SIW region and a coaxial region, connected by a radial port. The two regions are solved separately and then connected at the common radial port by their Generalized Admittance Matrices (GAM). On the common radial port, using a local cylindrical coordinate system (ρ, ϕ, z) centered at the center of the coaxial region, we define for the SIW and for the coaxial region a common excitation field in the form

$$\boldsymbol{E}_\xi = \boldsymbol{i}_z \sum_{m=0}^{M} \left\{ \begin{array}{c} \cos m\phi \\ \sin m\phi \end{array} \right. \tag{28}$$

For the coaxial region, if the material is the same in the SIW region and in the coaxial region ($\epsilon_{r,\mathrm{cx}} = \epsilon_{r,\mathrm{siw}}$ in Fig. 1), the computation of the GAM can be carried out as discussed in [22]. Since this case is completely documented in the cited paper, we discuss the case of unequal materials, which is also the most common case. For this case we use FEM in cylindrical coordinates to compute the GAM of

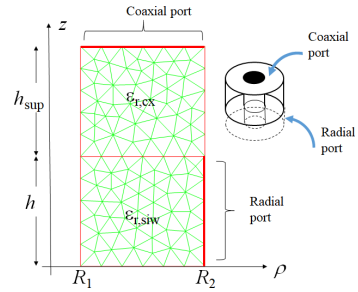

Fig. 2. An example of the mesh for the coaxial region, together with the ports used for GAM computation.

the coaxial region. Cylindrical coordinates are clearly very advantageous in this case, because each circular harmonic is solved separately. An example of the mesh for the coaxial region is shown in Fig. 2. The mesh is a 2D mesh in ρ, z plane and the problem is 2.5D, since the ϕ dependency is not constant. Note that the inner conductor of the coaxial cable is in contact with the bottom ground, since this is the most common configuration. A non contacting inner conductor can be implemented with no modifications in the formulation.

Using the cited local cylindrical coordinate system we assume in the cylindrical region a dependency of magnetic field in the form of a transverse-to-ϕ field $\boldsymbol{h}_t$ and a ϕ directed field $\boldsymbol{h}_\phi = \boldsymbol{i}_\phi h_\phi$, namely:

$$\boldsymbol{H}(\rho,\phi,z) = \sum_{m=0}^{M} \boldsymbol{h}_\phi^{(m)}(\rho,z) \left\{ \begin{array}{c} \cos m\phi \\ \sin m\phi \end{array} \right. + \sum_{m=0}^{M} \boldsymbol{h}_t^{(m)}(\rho,z) \left\{ \begin{array}{c} \cos(m\phi - \pi/2) \\ \sin(m\phi - \pi/2) \end{array} \right. \tag{29}$$

in which we indicate with superscript (m) the harmonic field component. Note that, contrary to the previous section, we now use subscript t to indicate transverse to ϕ. Eq. (29) is quite general but when applied to a body of revolution (such as the coaxial feed) it provides a complete decoupling of the various circular harmonics, so that the 3D problem is decomposed into $M+1$ problems in 2D, one for each value of parameter m (it can be shown the the two terms in parenthesis correspond to the same 2.5D problem). In our case the value of M is very small and we found excellent results for $M = 1$. The weak form for magnetic field is similar to (3) and reads:

$$\int_V \frac{1}{\epsilon_r} \nabla\times\boldsymbol{T}\cdot\nabla\times\boldsymbol{H}dV - k_0^2 \int_V \boldsymbol{T}\cdot\boldsymbol{H}dV = j\omega\epsilon_0 \int_{\partial V} \boldsymbol{T}\cdot\boldsymbol{E}_\xi \times \boldsymbol{i}_\nu dS \tag{30}$$

where $\boldsymbol{T}$ is a generic testing function, $\boldsymbol{i}_\nu$ is the outward drawn normal unit vector, $\boldsymbol{E}_\xi$ is the externally applied electric field, $dV = \rho d\phi d\rho dz$ and $dS = R_2 d\phi dz$ for the radial port (see Fig. 1) and $dS = \rho d\phi d\rho$ for the coaxial port. It is easily demonstrated that the different terms in (29) corresponding to different values of parameter m (different circular harmonics) are mutually orthogonal because of the integrals in ϕ and

therefore each circular harmonic corresponds to a separate FEM problem. In more detail, using (29) and letting

$$\boldsymbol{E}_\xi^{(m)} = \boldsymbol{e}_\xi^{(m)}(\rho, z) c_{m\phi} \tag{31}$$

be the excitation field for circular harmonic m, where $c_{m\phi} = \cos m\phi$ (only the upper term in the curly bracket in (29) and (31) is shown because the final equation is the same for both the upper term and the lower term in parenthesis), one finds that

$$\nabla \times (\boldsymbol{h}_\phi^{(m)} c_{m\phi}) = \frac{1}{\rho} \nabla_t \tilde{h}_\phi^{(m)} \times \boldsymbol{i}_\phi c_{m\phi} \tag{32}$$

$$\nabla \times (\boldsymbol{h}_t^{(m)} c_{m\phi_0}) = \nabla_t \times (\boldsymbol{h}_t^{(m)} c_{m\phi_0}) + \frac{m}{\rho} \boldsymbol{i}_\phi \times \boldsymbol{h}_t^{(m)} c_{m\phi} \tag{33}$$

where where $c_{m\phi_0} = \cos(m\phi - \pi/2)$, $\tilde{h}_\phi^{(m)} = \rho h_\phi^{(m)}$ and where we introduced the transverse-to-ϕ nabla operator

$$\nabla_t = \boldsymbol{i}_\rho \partial_\rho + \boldsymbol{i}_z \partial_z. \tag{34}$$

The weak form can now be specialized to the value of parameter m as follows: we define two types of testing functions, $\boldsymbol{t}_\phi(\rho, z) c_{m\phi}$ (directed along ϕ) and $\boldsymbol{t}_t(\rho, z) c_{m\phi_0}$ (in the transverse ρ, z plane) having the same dependence on ϕ as the corresponding magnetic field components. Testing the weak form (30) with these functions and carrying out the integrals in ϕ one finds that only terms corresponding to the same value of parameter m survive. For those terms, we end up with the following two ϕ-independent functional equations:

$$\int_S \left(\nabla_t \times \boldsymbol{t}_t \cdot \nabla_t \times \boldsymbol{h}_t^{(m)} + \frac{m^2}{\rho^2} \boldsymbol{t}_t \cdot \boldsymbol{h}_t^{(m)} - \frac{m}{\rho^2} \boldsymbol{t}_t \cdot \nabla_t \tilde{h}_\phi^{(m)} - k_0^2 \boldsymbol{t}_t \cdot \boldsymbol{h}_t^{(m)} \right) \frac{\rho}{\epsilon_r} d\rho dz = 0. \tag{35}$$

$$\int_S \left(-\frac{m}{\rho^2} \nabla_t \tilde{t}_\phi \cdot \boldsymbol{h}_t^{(m)} + \frac{1}{\rho^2} \nabla_t \tilde{t}_\phi \cdot \nabla_t \tilde{h}_\phi^{(m)} - k_0^2 \boldsymbol{t}_\phi \cdot \boldsymbol{h}_\phi^{(m)} \right) \frac{\rho}{\epsilon_r} d\rho dz = j\omega\epsilon_0 \int_L \boldsymbol{t}_\phi \cdot (\boldsymbol{e}_\xi^{(m)} \times \boldsymbol{i}_\nu) \rho dl \tag{36}$$

where $\tilde{t}_\phi = \rho t_\phi$. These are the equations we discretize and we point out that they are 2D equations involving line integrals and surface integrals and relaying on a 2D mesh. The discretization with Galerkin's method is now discussed in some detail.

C. FEM Discretization and GAM Computation for the Coaxial Region

For the solution of (35) associated to parameter m we use the following mixed expansion:

$$\rho h_\phi^{(m)}(\rho, z) = \sum_{q'} I_{\phi,q'}^{(m)} N_{q'}(\rho, z) \tag{37}$$

$$\boldsymbol{h}_t^{(m)}(\rho, z) = \sum_{q''} I_{t,q''}^{(m)} \boldsymbol{\tau}_{q''}(\rho, z) \tag{38}$$

where $N_{q'}$ are standard Lagrange node elements and $\boldsymbol{\tau}_{q''}$ are edge elements of matching degree [23]. From (37)–(38) one also finds that

$$\nabla \times \boldsymbol{i}_\phi \left(\frac{N_{q'}}{\rho} c_{m\phi} \right) = \frac{\nabla_t N_{q'} \times \boldsymbol{i}_\phi}{\rho} c_{m\phi} \tag{39}$$

$$\nabla \times (\boldsymbol{\tau}_{q''} c_{m\phi_0}) = \nabla_t \times \boldsymbol{\tau}_{q''} c_{m\phi_0} + \frac{m}{\rho} \boldsymbol{i}_\phi \times \boldsymbol{\tau}_{q''} c_{m\phi}. \tag{40}$$

Using Galerkin's method the weak form (35) associated to the generic parameter m is converted to the following matrix equation:

$$\left\{ \begin{bmatrix} \mathbf{A}'_{tt} + m^2 \mathbf{A}''_{tt} & m\mathbf{A}_{t\phi} \\ m\mathbf{A}_{\phi t} & \mathbf{A}_{\phi\phi} \end{bmatrix} - k_0^2 \begin{bmatrix} \mathbf{B}_{tt} & \mathbf{0} \\ \mathbf{0} & \mathbf{B}_{\phi\phi} \end{bmatrix} \right\} \begin{bmatrix} \mathbf{I}_t^{(m)} \\ \mathbf{I}_\phi^{(m)} \end{bmatrix} = j\omega\epsilon_0 \begin{bmatrix} \mathbf{0} \\ \mathbf{C}_\phi \end{bmatrix} \tag{41}$$

where $\mathbf{I}_t^{(m)} = [I_{t,1}^{(m)} I_{t,2}^{(m)} \ldots]^{\mathrm{T}}$, $\mathbf{I}_\phi^{(m)} = [I_{\phi,1}^{(m)} I_{\phi,2}^{(m)} \ldots]^{\mathrm{T}}$,

$$\mathbf{A}'_{tt}(p, q) = \int_S \frac{\nabla_t \times \boldsymbol{\tau}_p \cdot \nabla_t \times \boldsymbol{\tau}_q}{\epsilon_r} \rho d\rho dz \tag{42}$$

$$\mathbf{A}''_{tt}(p, q) = \int_S \frac{\boldsymbol{\tau}_p \cdot \boldsymbol{\tau}_q}{\epsilon_r \rho} d\rho dz \tag{43}$$

$$\mathbf{A}_{\phi t}(p, q) = -\int_S \frac{\nabla_t N_p \cdot \boldsymbol{\tau}_q}{\epsilon_r \rho} d\rho dz \tag{44}$$

$$\mathbf{A}_{t\phi}(p, q) = -\int_S \frac{\boldsymbol{\tau}_p \cdot \nabla_t N_q}{\epsilon_r \rho} d\rho dz \tag{45}$$

$$\mathbf{A}_{\phi\phi}(p, q) = \int_S \frac{\nabla_t N_p \cdot \nabla_t N_q}{\epsilon_r \rho} d\rho dz \tag{46}$$

$$\mathbf{B}_{tt}(p, q) = \int_S \boldsymbol{\tau}_p \cdot \boldsymbol{\tau}_q \, \rho d\rho dz \tag{47}$$

$$\mathbf{B}_{\phi\phi}(p, q) = \int_S \frac{N_p N_q}{\rho} d\rho dz \tag{48}$$

and for the radial port

$$\mathbf{C}_\phi(p, 1) = \int_0^h N_p dz \tag{49}$$

whereas for the coaxial port, only when $m = 0$,

$$\mathbf{C}_\phi(p, 1) = -\left[\ln \frac{R_2}{R_1} \right]^{-\frac{1}{2}} \int_{R_1}^{R_2} \frac{N_p}{\rho} d\rho \tag{50}$$

where R_2 and R_1 are respectively the outer and inner radius of the coaxial port. At the coaxial port $\mathbf{C}_\phi(p, 1) = 0$ for $m > 0$. Rewriting (41) as

$$\mathbf{L}^{(m)} \begin{bmatrix} \mathbf{I}_t^{(m)} \\ \mathbf{I}_\phi^{(m)} \end{bmatrix} = j\omega\epsilon_0 \begin{bmatrix} \mathbf{0} \\ \mathbf{C}_\phi \end{bmatrix} \tag{51}$$

one finds

$$\begin{bmatrix} \mathbf{I}_t^{(m)} \\ \mathbf{I}_\phi^{(m)} \end{bmatrix} = j\omega\epsilon_0 [\mathbf{L}^{(m)}]^{-1} \begin{bmatrix} \mathbf{0} \\ \mathbf{C}_\phi \end{bmatrix}. \tag{52}$$

Finally, the expression of the admittance matrix $\mathbf{Y}^{(m)}$ for the coaxial region is

$$\mathbf{Y}^{(m)} = \mathbf{C}_\phi^{\mathrm{T}} \mathbf{I}_\phi^{(m)}. \tag{53}$$

As a final notice, using the lower term in curly bracket in (29) one gets the exact same problem and therefore the same result for the GAM.

V. Admittance Matrix Connection and Scattering Matrix Computation

The admittance matrix (26) is the final admittance matrix $\mathbf{Y}^{\text{tot}}$ if only waveguide ports are present, and we can write

$$\mathbf{Y}^{\text{tot}} = \mathbf{Y}. \tag{54}$$

If one or more coaxial ports are present, in addition to the standard waveguide ports we have in the SIW region one radial port for each coaxial port (see Fig. 1). We can therefore split the admittance matrix in blocks as

$$\mathbf{Y} = \begin{bmatrix} \mathbf{Y}_{\text{wg,wg}} & \mathbf{Y}_{\text{wg,rad}} \\ \mathbf{Y}_{\text{rad,wg}} & \mathbf{Y}_{\text{rad,rad}} \end{bmatrix} \tag{55}$$

in which $\mathbf{Y}_{\text{wg,wg}}$ is the admittance submatrix for the waveguide ports only, $\mathbf{Y}_{\text{wg,rad}}$ and $\mathbf{Y}_{\text{rad,wg}}$ are the mutual admittance submatrices between waveguide ports and radial ports and $\mathbf{Y}_{\text{rad,rad}}$ is the admittance submatrix of the radial ports only. From [22] or using the procedure described in the previous section, we compute the admittance matrix $\mathbf{Y}^{(m)}$ for each harmonic m in the coaxial regions. Matrix $\mathbf{Y}^{(m)}$ can be partitioned as

$$\mathbf{Y}^{(m)} = \begin{bmatrix} \mathbf{Y}^{(m)}_{\text{rad,rad}} & \mathbf{Y}^{(m)}_{\text{rad,cx}} \\ \mathbf{Y}^{(m)}_{\text{cx,rad}} & \mathbf{Y}^{(m)}_{\text{cx,cx}} \end{bmatrix} \tag{56}$$

in which again subscript 'rad' refers to the radial port and 'cx' to the coaxial port. We introduce now

$$\mathbf{Y}' = \begin{bmatrix} \mathbf{Y}'_{\text{rad,rad}} & \mathbf{Y}'_{\text{rad,cx}} \\ \mathbf{Y}'_{\text{cx,rad}} & \mathbf{Y}'_{\text{cx,cx}} \end{bmatrix} \tag{57}$$

as the total admittance matrix of the coaxial region, obtained by assembling the various $\mathbf{Y}^{(m)}_{a,b}$ for all harmonics. The assembly process builds the following matrices:

$$\mathbf{Y}'_{\text{rad,rad}} = \begin{bmatrix} \mathbf{Y}^{(0)}_{\text{rad,rad}} & 0 & \cdots & \\ 0 & \mathbf{Y}^{(1,1)}_{\text{rad,rad}} & 0 & \cdots \\ \cdots & 0 & \mathbf{Y}^{(2,2)}_{\text{rad,rad}} & \cdots \\ & & & \ddots \end{bmatrix} \tag{58}$$

$$\mathbf{Y}'_{\text{cx,rad}} = \begin{bmatrix} \mathbf{Y}^{(0)}_{\text{cx,rad}} & \mathbf{Y}^{(1)}_{\text{cx,rad}} & \mathbf{Y}^{(1)}_{\text{cx,rad}} & \mathbf{Y}^{(2)}_{\text{cx,rad}} & \cdots \end{bmatrix} \tag{59}$$

$$\mathbf{Y}'_{\text{rad,cx}} = \left[\mathbf{Y}'_{\text{cx,rad}}\right]^T \tag{60}$$

$$\mathbf{Y}'_{\text{cx,cx}} = \mathbf{Y}^{(0)}_{\text{cx,cx}} \tag{61}$$

where

$$\mathbf{Y}^{(m,m)}_{\text{rad,rad}} = \begin{bmatrix} \mathbf{Y}^{(m)}_{\text{rad,rad}} & 0 \\ 0 & \mathbf{Y}^{(m)}_{\text{rad,rad}} \end{bmatrix}. \tag{62}$$

Note that, except for case $m = 0$, each harmonic-related submatrix is repeated twice to account for both polarizations (both terms in parenthesis in (29)). For the coaxial port self-term, only $\mathbf{Y}^{(0)}_{\text{cx,cx}}$ needs be computed (case $m = 0$), since higher order evanescent modes coefficients at the coaxial port can be made arbitrarily small by choosing h_{sup} in Fig. 1 sufficiently large ($h_{\text{sup}} \simeq 2R_2$ is usually sufficient). The size of matrix $\mathbf{Y}'$ for each coaxial port is then $2M+2$ since there are $2M+1$ radial ports and 1 coaxial port. A corresponding sorting and assembling is carried out on $\mathbf{Y}_{\text{rad,rad}}$, so that matrices can be connected with matching azimuthal index and polarization.

We can now obtain the final admittance matrix $\mathbf{Y}^{\text{tot}}$ of the SIW that includes the case of coaxial ports as

$$\mathbf{Y}^{\text{tot}} = \begin{bmatrix} \mathbf{Y}^{\text{tot}}_{\text{wg,wg}} & \mathbf{Y}^{\text{tot}}_{\text{wg,cx}} \\ \mathbf{Y}^{\text{tot}}_{\text{cx,wg}} & \mathbf{Y}^{\text{tot}}_{\text{cx,cx}} \end{bmatrix} \tag{63}$$

where

$$\mathbf{Y}^{\text{tot}}_{\text{wg,wg}} = \mathbf{Y}_{\text{wg,wg}} - \mathbf{Y}_{\text{wg,rad}}\mathbf{Z}\mathbf{Y}_{\text{rad,wg}} \tag{64}$$

$$\mathbf{Y}^{\text{tot}}_{\text{cx,cx}} = \mathbf{Y}'_{\text{cx,wg}} - \mathbf{Y}'_{\text{cx,rad}}\mathbf{Z}\mathbf{Y}'_{\text{rad,cx}} \tag{65}$$

$$\mathbf{Y}^{\text{tot}}_{\text{wg,cx}} = -\mathbf{Y}_{\text{wg,rad}}\mathbf{Z}\mathbf{Y}'_{\text{rad,cx}} \tag{66}$$

$$\mathbf{Y}^{\text{tot}}_{\text{cx,wg}} = -\mathbf{Y}'_{\text{cx,rad}}\mathbf{Z}\mathbf{Y}_{\text{rad,wg}} \tag{67}$$

and

$$\mathbf{Z} = (\mathbf{Y}_{\text{rad,rad}} + \mathbf{Y}'_{\text{rad,rad}})^{-1}. \tag{68}$$

A. Scattering Matrix

From the total admittance matrix we can obtain the scattering matrix $\mathbf{S}$ as

$$\mathbf{S} = -\sqrt{\mathbf{Y}_{\text{ref}}}(\mathbf{Y}_{\text{ref}} + \mathbf{Y}^{\text{tot}})^{-1}(\mathbf{Y}_{\text{ref}} + \mathbf{Y}^{\text{tot}})\sqrt{\mathbf{Z}_{\text{ref}}} \tag{69}$$

where $\mathbf{Y}_{\text{ref}}$ is the diagonal matrix of reference admittances at the ports and $\mathbf{Z}_{\text{ref}} = \mathbf{Y}^{-1}_{\text{ref}}$. For both waveguide ports and coaxial ports, the reference admittance matrix is the wave admittance. The generic element $\mathbf{Y}_{\text{ref}}(i)$ of the wave admittance is therefore

$$\mathbf{Y}_{\text{ref}}(i) = \left[\frac{\sqrt{(n_i\pi/a_i)^2 - k_0^2\epsilon_{r,\text{siw}}}}{j\omega\mu}\right] \tag{70}$$

being $\epsilon_{r,\text{siw}}$ the relative permittivity in the SIW region, n_i the mode index relative to index i and a_i the port size relative to index i. For the coaxial case we have then

$$\mathbf{Y}_{\text{ref}}(i) = \sqrt{\frac{\epsilon_0\epsilon_{r,\text{cx}}}{\mu_0}} \tag{71}$$

being $\epsilon_{r,\text{cx}}$ the relative permittivity in the upper coaxial region in Fig. 1.

VI. Results

The advantage of 2D FEM is clearly the reduced number of unknowns with respect to 3D FEM. As an example, using first order edge elements in a 2D mesh (linear elements), a total of eight functions per triangle are defined. On a tetrahedral grid, first order edge elements correspond to twenty functions in each tetrahedron [25] and since two tetrahedrons are needed to model the field on a triangular prism, the total number of functions per element is forty. Therefore the use of 2D FEM leads to great time savings and reduced memory storage for a given accuracy in the computation. Moreover, the use of circular arc elements to define the vias allows to avoid unnecessarily dense meshes. Finally, the temporary radial ports to represent coaxial input preserve the 2D nature of the problem and the accuracy in the computation.

The first example we show is a test of the radiation boundary condition represented by (12). In general radiation is negligible providing that the vias are close enough, the rule being dictated

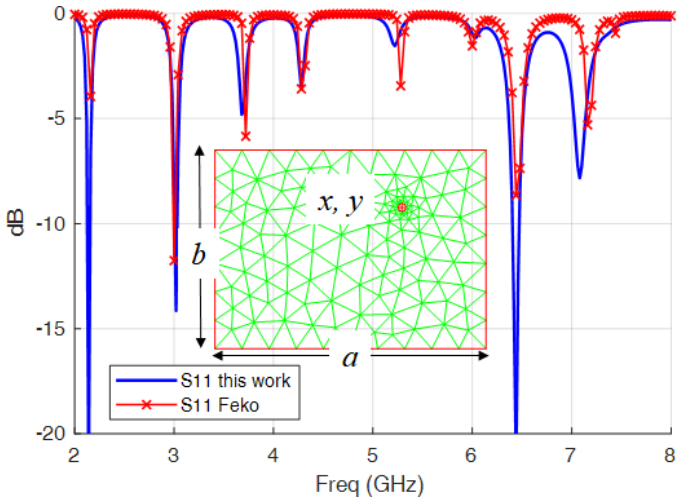

Fig. 3. Coaxial-fed rectangular resonator with open walls. Parameters are $a = 46.8$ mm, $b = 33.2$ mm, $(x, y) = (8.9, 7)$ mm with respect to the center, $h = 0.5$ mm (SIW thickness), $\epsilon_r = 2.2$ (SIW material), $\epsilon_r = 2.1$ (coaxial cable), $d = 0.4$ mm (inner diameter of coaxial cable). Comparison with Feko^{TM} citeFeko.

by the simple formula $s < 2d$, being s the spacing between vias (from the centers) and d the vias' diameter. The radiation boundary condition (12) can be useful to check for unwanted radiation. In order to test it in the extreme case of no vias, we have analyzed a simple patch resonator that is fed by a coaxial cable and compared the results obtained with Feko^{TM} [26]. The results obtained are shown in Fig. 3. Note that there is a reasonable agreement between the results obtained with the method in this work and Feko. The various resonances of the structure are represented quite well and we found that eq. (12) can be successfully used as an approximate check for possible spurious radiation from the structure.

The next example is a waveguide-fed SIW filter. The filter has been designed in [12] and analyzed by Bi-RME and 3D FEM. The comparison between our code and 3D FEM (HFSS^{TM} [27]) is shown in Fig. 4. The material parameters are $\epsilon_r = 2$, $\tan\delta = 0.0011$ and $\sigma = 4 \cdot 10^7$ S/m. An excellent agreement is observed, for the center frequency, the return loss level and the insertion loss. Thanks to the use of circular arc elements it was possible to keep the mesh density to a very reasonable size, with 1271 triangles and 6640 degrees of freedom (dof) using linear edge elements (degree 1 along the edge). The analysis took 0.034 sec/freq with a Matlab implementation of the code running on an Intel i7 pc with 4 GHz clock rate.

As a further test on the radiation boundary condition we analyzed the same filter with just 6 vias per side and results are shown in Fig. 5, together with results obtained by HFSS. The main effect observed is a significant shift in the center frequency. This is correctly modeled also with the method discussed in this work. Note that in this case the rule $s < 2d$ to keep radiation small is not fulfilled, and the SIW structure is far from optimal. In spite of that, radiation effects are negligible since from the simulations the insertion loss level is almost unchanged and the only observable effect is the cited frequency shift. Because of the approximate nature of (12)

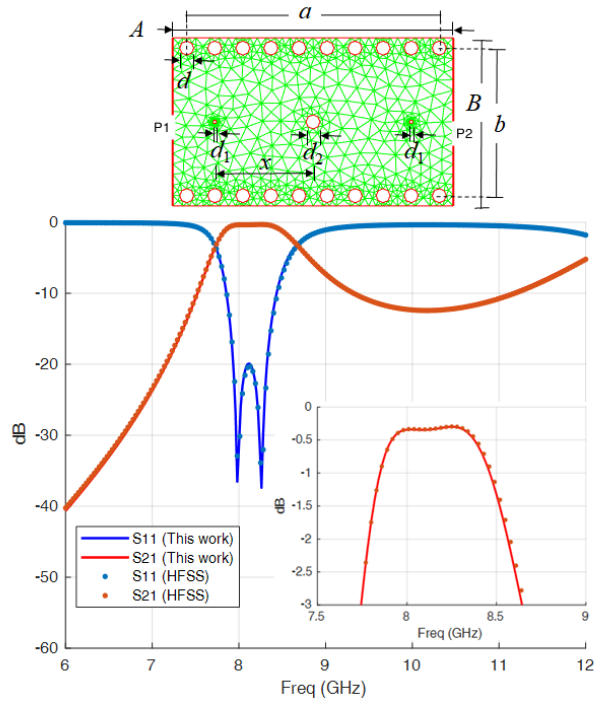

Fig. 4. Waveguide-fed SIW filter with two resonators. Data from [12] (mm): $A = 40$, $B = 24$, $a = 36$, $b = 21.06$, $d = d_2 = 2$, $d_1 = 0.5$, $x = 14$, $h = 1$, $\epsilon_r = 2(1 - j0.0011)$. Comparison between results obtained in this work and HFSS. A closeup of the passband region is shown as an inset.

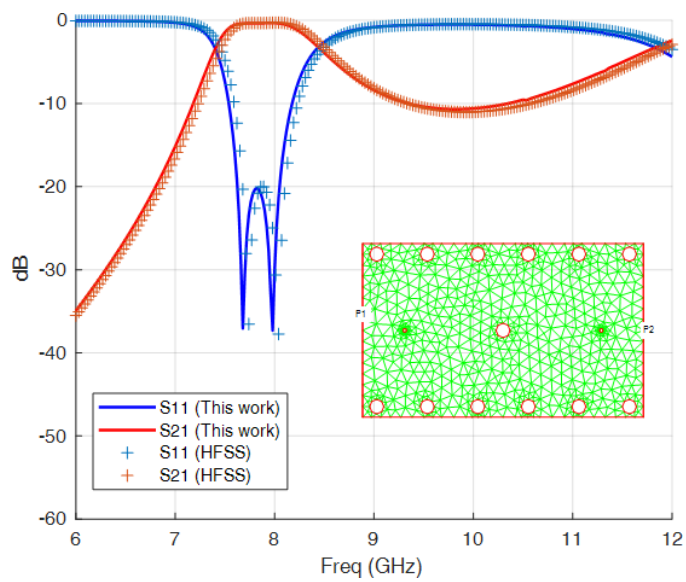

Fig. 5. Waveguide-fed SIW filter with two resonators, same dimensions as in Fig. 4 but with just 6 vias on the sides. Comparison between results obtained in this work and HFSS.

the agreement is not as good as in the previous case. HFSS analysis was setup so as to account for any radiation losses by enlarging the size of the structure and introducing absorbing boundary conditions.

The third example is a coaxial-fed filter that comprises air regions, realized by milling the SIW structure (Fig. 6). For the SIW we used a material with a high value of permittivity

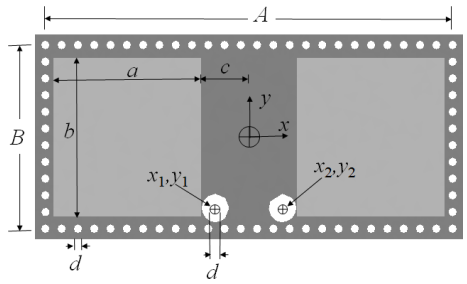

Fig. 6. Coaxial-fed SIW filter with air regions analyzed in Fig. 7. Length values in mm: $A = 50$, $B = 21.7$, $a = 11.7$, $b = 18.7$, $c = 5.85$, $x_1 = -4.1$, $y_1 = -8.4$, $x_2 = 4.1$, $y_2 = -8.4$, $d = 1$. Materials: $\epsilon_r = 1$ (light grey), $\epsilon_r = 10.2(1 - j0.003)$ (dark grey), $\epsilon_r = 2.1$ (coaxial cable), $\sigma = 5.8 \cdot 10^7$ S/m (conductors).

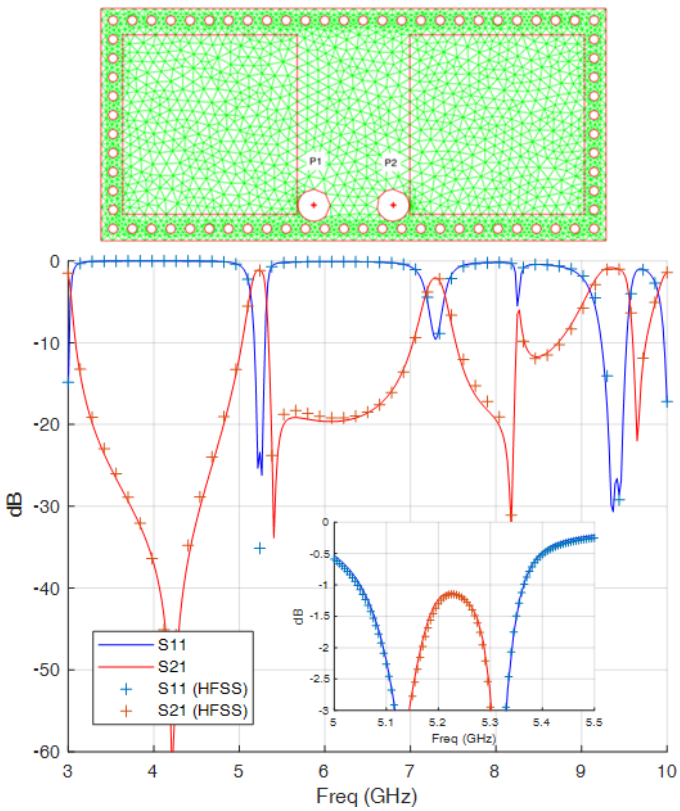

Fig. 7. Coaxial-fed SIW filter with air regions. Data are shown in Fig. 6. Comparison between results obtained in this work and HFSS. A closeup of the passband region is shown as an inset.

in the dielectric filled parts ($\epsilon_r = 10.2$, $\tan\delta = 0.003$, for conductors $\sigma = 5.8 \cdot 10^7$ S/m). In this example the number of triangles was 4017 and the total number of dofs was 20856 using linear edge elements. The agreement with HFSS results is very good over the wide bandwidth of analysis also for the insertion loss level (an inset in the figure). For this case we also carried out a comparison in terms of CPU time required for the analysis, even if the implementation of the method presented in this paper is far from optimal, since it has been carried out in Matlab. Even so, using HFSS the discrete sweep took 3.2 sec/freq whereas the analysis with the method presented in this paper took 0.32 sec/freq, corresponding to a speedup factor of 10.

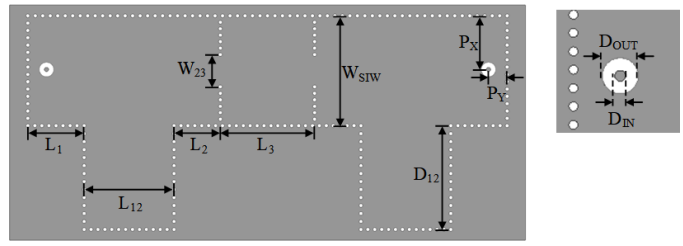

Fig. 8. The physical variables of the filter analyzed in Fig. 9. Length values are in mm. $L_1 = 15.69$, $L_2 = 12.91$, $L_3 = 26.26$, $L_{12} = 25.05$, $D_{12} = 28.90$, $W_{23} = 8.99$, $W_{\rm SIW} = 30.6$, $P_x = 14.961$, $P_y = 5.2$, $\epsilon_r = 2.2$ (SIW structure), $\tan\delta = 0.0009$ (loss tangent of SIW structure), $D_{\rm via} = 1$ (diameter of the vias), $h = 1.524$ (dielectric thickness of SIW), $D_{\rm out} = 4$, $D_{\rm in} = 1.2$, $\epsilon_r = 2.2$ (coaxial I/O structure), $\sigma = 3.5 \cdot 10^7$ S/m (conductivity of vias and ground planes).

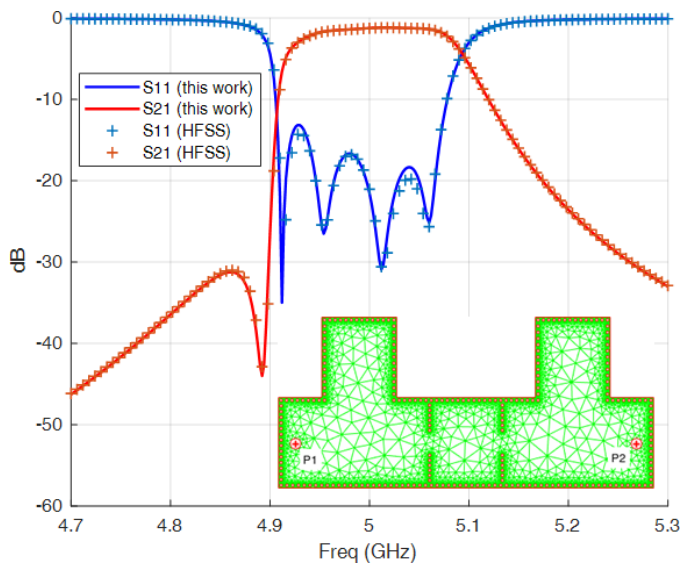

Fig. 9. Coaxial-fed SIW filter realizing a transmission zero by frequency-variant coupling. Comparison between results obtained in this work and HFSS. Material used for the SIW has $\epsilon_r = 2.2$, $\tan\delta = 0.0009$.

A further example is shown in Fig. 8-9. This filter represents the implementation of a transmission zero by frequency variant couplings [28]. The filter is fed with coaxial cables and the analysis is concentrated in the passband. The dielectric material has $\epsilon_r = 2.2$, $\tan\delta = 0.0009$ and for the conductors we used $\sigma = 3 \cdot 10^7$ S/m. The mesh used comprises 11123 triangles and the use of linear edge elements corresponded to 58226 dof's. As shown in Fig. 9, the agreement with the results of HFSS is excellent. HFSS results have been obtained with linear elements in 3D, so the degree of approximation is the same for both methods. The analysis took 0.57 sec/freq. By comparison, the discrete frequency sweep with HFSS (73987 tetrahedrons and 560150 dofs) took more than 9 sec/freq (speed up factor of about 15 using our code). This example, that represents a rather complex structure, is a good benchmark for the coaxial port model we have used and the good agreement of the results in the filter passband confirm the accuracy of the model.

As a final example we show a comparison with measured data from [29]. The comparison refers to a SIW cavity that is loaded with a textile material, whose parameters are $\varepsilon_r =$

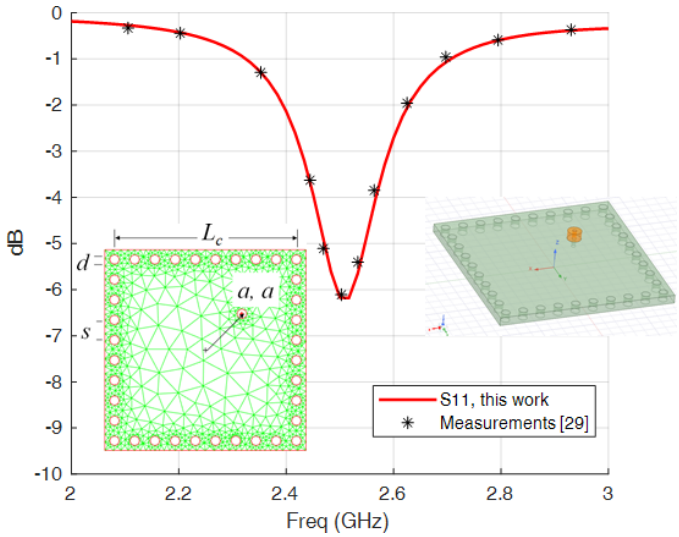

Fig. 10. Coaxial-fed SIW cavity. Dimensions in mm are: $L_c = 74.7$, $d = 4$ (diameter of vias), $s = 8$ (spacing of vias), $a = 15$ (offset from the center). Moreover we have $h = 3.94$ mm, $\varepsilon_r = 1.45$, $\tan\delta = 0.017$ for the internal material, $R_s = 0.18\ \Omega/\text{sq}$ at 2.45 GHz for the upper and lower conductors, $\sigma = 1.5 \cdot 10^7$ S/m for the vias. Comparison between reflection coefficient obtained in this work and measured value.

1.45, $\tan\delta = 0.017$. The purpose of the SIW cavity was to characterize losses in the textile material. The thickness of the material is $h = 3.94$ mm and the cavity dimensions are given in the inset of Fig. 10. For the upper and lower conductors Taffeta was used, with a surface resistivity $R_s = 0.18\ \Omega/\text{sq}$ at 2.45 GHz and the vias were realized in brass ($\sigma = 1.5 \cdot 10^7$ S/m). Parameter $|S_{11}|$ is computed by the method in this work and compared in Fig. 10 to the measured value and a very good agreement is observed. The SIW cavity is fed by a SMA connector with inner radius 0.6 mm and Teflon as a support material. Also in this case, virtually identical results have been obtained with HFSS software, but with a much larger computing time.

VII. Conclusions

A method for the analysis of SIW structures based on 2D vector Finite Element Method has been presented. The formulation used includes losses, inhomogeneous dielectric and excitation by rectangular waveguide or coaxial cable. A simple approximate expression for spurious radiation by the boundary has been introduced. Comparison with standard 3D FEM and with measured data has proven the excellent accuracy of the technique. Based on several analysis, we observed a speed up factor of the order of 10-20. Further work is being carried out for the inclusion of microstrip-type input, trying to preserve as much as possible the 2D nature of the problem.

References

[1] M. Bozzi, A. Georgiadis and K. Wu, "Review of substrate-integrated waveguide circuits and antennas," *IET Microwaves, Antennas Propagation*, vol. 5, no. 8, pp. 909-920, 6 June 2011, doi: 10.1049/iet-map.2010.0463.

[2] L. Silvestri, E. Massoni, C. Tomassoni, A. Coves, M. Bozzi and L. Perregrini, "Substrate Integrated Waveguide Filters Based on a Dielectric Layer With Periodic Perforations," *IEEE Transactions on Microwave Theory and Techniques*, vol. 65, no. 8, pp. 2687-2697, Aug. 2017.

[3] A. Ghiotto, "Air-filled substrate integrated waveguide: A low cost self-packadged technological platform for high performance millimeterwave circuits," in 2017 *Proc. IEEE 21st Workshop on Signal and Power Integrity* (SPI), 2017, pp. 1-2.

[4] J. Corsi et al., "Partially-Air-Filled Slow-Wave Substrate Integrated Waveguide in Metallic Nanowire Membrane Technology," in 2020 *Proc. IEEE/MTT-S International Microwave Symposium* (IMS), 2020, pp. 9-12.

[5] C. Tomassoni, L. Silvestri, A. Ghiotto, M. Bozzi and L. Perregrini, "Substrate-Integrated Waveguide Filters Based on Dual-Mode Air-Filled Resonant Cavities," *IEEE Transactions on Microwave Theory and Techniques*, vol. 66, no. 2, pp. 726-736, Feb. 2018.

[6] Á. Coves, G. Torregrosa, G. Vicent, E. Bronchalo, Á. A. San Blas and M. Bozzi, "Modeling of perforated SIW structures and their application to the design of step-impedance microwave filters," in 2017 *Proc. IEEE MTT-S International Conference on Numerical Electromagnetic and Multiphysics Modeling and Optimization for RF, Microwave, and Terahertz Applications* (NEMO), 2017, pp. 293-295.

[7] R. Beyer, P. W. Krauss and T. Sieverding, "Design of cross-coupled substrate integrated waveguide filters with the mode-matching and finite element methods," in 2015 *Proc. IEEE MTT-S International Conference on Numerical Electromagnetic and Multiphysics Modeling and Optimization* (NEMO), Ottawa, ON, 2015, pp. 1-3.

[8] M. A. Rabah, M. Abri, J. W. Tao and Tan-Hoa Vuong, "Substrate Integrated Waveguide Design Using the Two Dimensional Finite Element Method", *Progress In Electromagnetics Research M*, Vol. 35, 21-30, 2014.

[9] M. Li, K. Feng and R. Chen, "FEM full-wave analysis of substrate integrated waveguide with reduced model method," in 2011 *Proc. IEEE Electrical Design of Advanced Packaging and Systems Symposium* (EDAPS), Hanzhou, 2011, pp. 1-3.

[10] C. A. Leal-Sevillano, J. A. Ruiz-Cruz, J. R. Montejo-Garai and J. M. Rebollar, "A virtual lossy dielectric model with composite boundary conditions for the analysis of substrate integrated waveguides," in 2016 *Proc. 46th European Microwave Conference* (EuMC), London, 2016, pp. 162-165.

[11] J. Bornemann and S. S. Hesari, "Scattering matrix subtraction technique for mode-matching analysis of substrate integrated waveguide junctions," in 2017 *Proc. IEEE MTT-S International Conference on Numerical Electromagnetic and Multiphysics Modeling and Optimization for RF, Microwave, and Terahertz Applications* (NEMO), Seville, 2017, pp. 1-3.

[12] M. Bozzi, L. Perregrini and K. Wu, "Modeling of Conductor, Dielectric, and Radiation Losses in Substrate Integrated Waveguide by the Boundary Integral-Resonant Mode Expansion Method," *IEEE Transactions on Microwave Theory and Techniques*, vol. 56, no. 12, pp. 3153-3161, Dec. 2008.

[13] A. Belenguer, H. Esteban, E. Diaz, C. Bachiller, J. Cascon and V. E. Boria, "Hybrid Technique Plus Fast Frequency Sweep for the Efficient and Accurate Analysis of Substrate Integrated Waveguide Devices," *IEEE Transactions on Microwave Theory and Techniques*, vol. 59, no. 3, pp. 552-560, March 2011.

[14] E. Diaz. Caballero, H. Esteban, A. Belenguer and V. Boria, "Efficient Analysis of Substrate Integrated Waveguide Devices Using Hybrid Mode Matching Between Cylindrical and Guided Modes," *IEEE Transactions on Microwave Theory and Techniques*, vol. 60, no. 2, pp. 232-243, Feb. 2012.

[15] M. Casaletti, G. Valerio, R. Sauleau and M. Albani, "Mode-Matching Analysis of Lossy SIW Devices," *IEEE Transactions on Microwave Theory and Techniques*, vol. 64, no. 12, pp. 4126-4137, Dec. 2016.

[16] M. Casaletti, R. Sauleau, M. Ettorre and S. Maci, "Efficient Analysis of Metallic and Dielectric Posts in Parallel-Plate Waveguide Structures," *IEEE Transactions on Microwave Theory and Techniques*, vol. 60, no. 10, pp. 2979-2989, Oct. 2012.

[17] J. Rubio, A. G. García, R. G. Alcalá, Y. Campos-Roca and J. Zapata, "Overall Formulation for Multilayer SIW Circuits Based on Addition Theorems and the Generalized Scattering Matrix," *IEEE Microwave and Wireless Components Letter*s, vol. 28, no. 6, pp. 485-487, June 2018.

[18] Leontovich. M. A. 'Approximate boundary conditions for the electromagnetic field on the surface of a good conductor'. *Investigations on radiowave propagation*, Pt II, Printing House of the Academy of Sciences, Moscow, 1948.

[19] C. Balanis, *Antenna Theory, Analysis and Design* (4th Edition), Wiley, New York, 2016.

[20] G. G. Gentili, L. Accatino and G. Bertin, "The Generalized 2.5-D Finite-Element Method for Analysis of Waveguide Components," *IEEE Transactions on Microwave Theory and Techniques*, vol. 64, no. 8, pp. 2392-2400, Aug. 2016.

[21] Z. Kordiboroujeni and J. Bornemann, "Designing the Width of Substrate Integrated Waveguide Structures," *IEEE Microwave and Wireless Components Letters*, vol. 23, no. 10, pp. 518-520, Oct. 2013.

[22] G. G. Gentili, "Multiport analysis of arbitrary circular-rod insets in rectangular waveguide by the generalized admittance matrix," *IEEE Transactions on Microwave Theory and Techniques*, vol. 49, no. 8, pp. 1438-1442, Aug. 2001.

[23] G. G. Gentili, P. Bolli, R. Nesti, G. Pelosi and L. Toso, "High-Order FEM Mode Matching Analysis of Circular Horns With Rotationally Symmetric Dielectrics," *IEEE Transactions on Antennas and Propagation*, vol. 55, no. 10, pp. 2915-2918, Oct. 20076.

[24] L. Codecasa, G. G. Gentili, M. Khosronejad, G. Pelosi, S. Selleri, "Exact conic section arc elements in 2D and 2.5D FEM using a coordinate transformation", *IET microwaves, antennas & propagation*, 2021-07-29, Vol.15 (9), p.1108-1116.

[25] R. D. Graglia, D. R. Wilton and A. F. Peterson, "Higher order interpolatory vector bases for computational electromagnetics," *IEEE Transactions on Antennas and Propagation*, vol. 45, no. 3, pp. 329-342, March 1997.

[26] Altair Feko, Altair Engineering, Inc., www.altairhyperworks.com/feko.

[27] Ansys® Electronic Desktop, Release 2021 R2.

[28] G. Macchiarella, G. G. Gentili, N. Delmonte, L. Silvestri and M. Bozzi, "Design of Inline Waveguide Filters With Frequency-Variant Couplings Producing Transmission Zeros," *IEEE Transactions on Microwave Theory and Techniques*, vol. 69, no. 8, pp. 3746-3758, Aug. 2021.

[29] R. Moro, S. Agneessens, H. Rogier, A. Dierck and M. Bozzi, "Textile Microwave Components in Substrate Integrated Waveguide Technology," *IEEE Transactions on Microwave Theory and Techniques*, vol. 63, no. 2, pp. 422-432, Feb. 2015.